



HAL
open science

Generating STL for forming trabecular bone structure in additive manufacturing using cell dynamics modeling

Adones Almeida Rocha, Rossana Mara da Silva Thiré, Anna Carla Araujo

► To cite this version:

Adones Almeida Rocha, Rossana Mara da Silva Thiré, Anna Carla Araujo. Generating STL for forming trabecular bone structure in additive manufacturing using cell dynamics modeling. ESAFORM 2023, AGH University of Science and Technology, Apr 2023, Kracov, Poland. hal-04001676

HAL Id: hal-04001676

<https://hal.science/hal-04001676>

Submitted on 23 Feb 2023

HAL is a multi-disciplinary open access archive for the deposit and dissemination of scientific research documents, whether they are published or not. The documents may come from teaching and research institutions in France or abroad, or from public or private research centers.

L'archive ouverte pluridisciplinaire **HAL**, est destinée au dépôt et à la diffusion de documents scientifiques de niveau recherche, publiés ou non, émanant des établissements d'enseignement et de recherche français ou étrangers, des laboratoires publics ou privés.

Generating STL for forming trabecular bone structure in additive manufacturing using cell dynamics modeling

Adones A. Rocha ^{1,a*},

Rossana M.S.M. THIRÉ ^{1,2,b} and

Anna-Carla ARAUJO ^{2,c}

¹Alberto Luiz Coimbra Institute for Graduate Studies and Research in Engineering/Metallurgical and Material Engineering Program (PEMM/COPPE), Federal University of Rio de Janeiro, Brazil

²Institut Clément Ader, Université de Toulouse, CNRS/INSA/ISAE/Mines Albi/UPS, France

^aadones.rocha@coppe.ufrj.br, ^brossana@metalmat.ufrj.br, ^caraujo@insa-toulouse.fr

Keywords: Additive Manufacturing, FFF, Biopolymers, STL generation, Trabecular Bone.

Abstract. There are two types of structures in bone with different densities: cortical bone, a denser region, and trabecular bone, a porous part. Poly(lactic acid) - PLA, a biopolymer widely used in additive manufacturing (AM), can be applied for fabricate products for medical and dental applications since it is biodegradable and biocompatible to several mammalian cell lines. This article proposes a methodology for generating STL to produce by AM a structure with geometry similar to that of trabecular bone using a mathematical model that describes the population dynamics of bone cells. Bone density values obtained by solving the differential equations model with finite differences are used to develop a mesh surface. This surface is converted into a binarized mesh using a binary algorithm and, finally, the STL file is obtained by applying the multidimensional arrays tool from Matlab® software. The produced file is analyzed by BoneJ® using the same procedure currently applied for bone tomography to obtain some geometry parameters as trabecular thickness, trabecular separation, bone fraction and connectivity; and the degree of anisotropy. 3D Printed samples were successfully produced by Fused Filament Fabrication (FFF) using PLA filament. It was noticed that the produced structure is similar to the morphology of the trabecular part of the femoral head, comparing the different strategies of obtain STL and real bone tomography.

Introduction

Bone architecture can be classified as cortical or trabecular. Cortical bone is made up of a compact region of mineralized material, while trabecular bone has structures known as trabeculae, which are highly porous [1]. Bone is a mineralized conjunctive tissue that exhibits four types of cells: osteoblasts, osteocytes, osteoclasts, and bone lining cells [2]. Bone composition is given by 50-70% of inorganic material (hydroxyapatite), 20-40% of organic material (collagen I), and 5-10% of water and other materials, such as lipids and fibrillin [3].

The trabecular region of the bone is the most affected by fractures and is the area where bone weakening can happen with different carcinomas and pathologies. However, more facts need to be clarified about the characteristics of this tissue region, as well as the strategies to reproduce it aiming as a replacing bone tissue (bone tissue engineering) and technical-academic studies (orthopedic surgeries).

It is noticed many techniques to reproduce the trabecular bone structure as capture and image processing using computed tomography that stands out as a gold standard [4]. This process is relatively high cost and it need for real experiments, so the use of mathematical models as Wolff and Roux laws is an alternative to obtain this architecture as a digital image. These mathematical approaches describe the architecture of trabeculae as responses to mechanical stimuli [4]. Recent progress has shown that this approach can be considered outdated since bone architecture can be related to cell effects [4] and bone cell remodeling [5].

A mathematical model developed by Komarova *et al.* [1] describes the dynamics of bone cells population, in view osteoclasts and osteoblasts in a basic multicellular unit. The authors explain the effect of local regulatory factors on cell production rates, employing a power law approximation. A system of differential equations is defined for variations in cell population (osteoblasts and osteoclasts) and bone mass. This model has been used in recent years in several studies to describe different phenomena and bone pathologies. Ayati *et al.* [6] adapted the mathematical modeling of Komarova *et al.* [1] to study the healthy cell population and those with tumor cells. In this paper, the cell diffusion and bone density

were evaluated, with cell and bone density are described in one dimension. Valério et al. [7] investigated using the model to the anomalous (tumor) and healthy growth of the bone mass, considering disturbances in the origin, and applying the method of finite differences in two dimensions. Peyroteo *et al.* [8] studied the application of the finite element method to solve the remodeling equations and analyze the results in conditions of healthy bone and osteoporosis.

The work of Fernández-Cervantes *et al.* [9] applying the space-time adaptations of Ayati *et al.* [6] proposes to solve the system of differential equations using Euler's method for the temporal part and the finite difference method for the spatial part, to obtain a porous piece with a structure like the trabecular bone. Then, the authors used the 3D printing binder jetting technique to obtain printed pieces. The authors found patterns and profiles similar to those of trabecular bone morphology by assessing the image produced with the patterns of real trabecular bone.

In the image processing analysis of the trabecular bone structure, some parameters are important as defined by McGregor *et al.* [10]: Trabecular Thickness, Trabecular Separation, Bone Volume Fraction, Degree of Anisotropy and Connectivity. These parameters can be analyzed to mimic the trabecular structure, knowing that the study of Trabecular Thickness and Trabecular Separation dispersion in a certain range of values is important, since real bone does not have isotropic trabecular thickness and separation [11]. These characteristics of bone morphology may be key factors for tissue compatibility and regeneration when applied to tissue engineering scaffolds.

Filament Fusion Fabrication (FFF) is a simple 3D printing technique and relatively cheap when compared to other techniques that have greater precision [12]. In this technique, it is possible to obtain, with a 0.2 mm nozzle, structures that simulate a corresponding trabecular thickness of 0.2 mm. Most of the bones in the human body have thin trabecular, however, the femoral head bone has an average trabecular thickness of 0.19 mm, being the thickest documented [10]. Therefore, these structures have the potential to be printed by FFF, despite the relatively low accuracy of the technique compared to more robust AM techniques. Obtaining files that can be read by 3D printer software is essential for the operation of the technique, such as STL files that describe the surface with triangulation [12]. The present work seeks to apply the mathematical model proposed for cellular remodeling to obtain a STL that mimics the bone trabecular structure, for so it is analyzed the different bone parameters in comparison with real bone of femoral head in pieces printed by FFF.

Modeling the bone dynamics

Bone is a mineralized conjunctive tissue that exhibits four types of cells: osteoblasts, osteocytes, osteoclasts, and bone lining cells. This tissue performs important functions in the body, such as locomotion, support, and protection of soft tissues, calcium and phosphate storage, and bone marrow shelter. Despite its immobile appearance, bone is a highly dynamic organ. Bone material is continuously reabsorbed by osteoclasts and "rebuilt" by osteoblasts [8].

The model of bone remodeling proposed by Komarova *et al.* [1] takes into account that both osteoclasts and osteoblasts can produce local factors capable of activating or inhibiting themselves, or activating or inhibiting another cell type, i.e., signaling respectively autocrine and paracrine factors. A simplified hypothesis considers that autocrine and paracrine factors only regulate the production rate of osteoclasts and osteoblasts and their removal rates are proportional to the current number of corresponding cells. Some growth factors were neglected, such as the action of the nuclear factor kappa β ligand-receptor activator (RANKL) and insulin (IGF) that can promote osteoclasts and osteoblasts survival. These assumptions reduced the number of parameters helping its implementation.

Equations (1) and (2) present the Komarova model describing the dynamics of cell populations for bone remodeling along the time (t). The main variables of the model are: number of cells of osteoclasts (C), number of cells of osteoblasts (B) and bone mass (ρ).

$$\frac{dC(t)}{dt} = \alpha_1 C(t)^{g_{11}} B(t)^{g_{21}} - \beta_1 C(t), \quad (1)$$

$$\frac{dB(t)}{dt} = \alpha_2 C(t)^{g_{12}} B(t)^{g_{22}} - \beta_2 B(t). \quad (2)$$

The constants α_i and β_i are called as cell production and removal activities, respectively, and $g_{i,j}$ represents the efficacy of autocrine or paracrine factors derived from osteoclasts (index 1) or osteoblasts (index 2).

Komarova model also propose Eq. 3 to calculate the bone mass $\rho(t)$ as a function of the cell population in steady state ($t \rightarrow \infty$), the constants are k_i that corresponds to the normalized activity of bone resorption (index C) and formation (index B). The term inside the parentheses in Eq. 3 corresponds to the number of cells that actively resorb or form bone, and the variables \underline{C} and B indicate the values of number of cells in steady-state.

$$\frac{d\rho(t)}{dt} = -k_c(t)\max(0, C(t) - \underline{C}) + -k_B(t)\max(0, B(t) - \underline{B}). \quad (3)$$

To obtain estimates of the initial parameters, Komarova *et al.* used experimental data obtained from the histomorphometry analysis of bone sections [1].

A second model is proposed by Ayati *et al.* [6], an extended mathematical model adding a diffusion cells term (D_i), that it is multiply by the Laplacian of cell number, obtaining a field with cell population. The spatial distribution of $C(t)$, $B(t)$ and $\rho(t)$ is calculated using Eq. 5, 6 and 7, where $u = (x, y, z)$. A numerical finite difference method can be used to solve this system.

$$\frac{\partial C(u, t)}{\partial t} = D_C \nabla^2 C(u, t) + \alpha_1 C(u, t)^{g^{11}} B(u, t)^{g^{21}} - \beta_1 C(u, t), \quad (5)$$

$$\frac{\partial B(u, t)}{\partial t} = D_B \nabla^2 B(u, t) + \alpha_2 C(u, t)^{g^{12}} B(u, t)^{g^{22}} - \beta_2 B(u, t), \quad (6)$$

$$\frac{\partial \rho(u, t)}{\partial t} = -k_1(u, t)\max(0, C(u, t) - \underline{C}) + k_2\max((u, t) - \underline{B}). \quad (7)$$

Methodology for STL surface using cells models

Two strategies (S1) and (S2) were developed in this article to produce the three-dimensional surfaces based on the presented models. The same cubic envelop was used for both strategies wherein bone and porous regions were produced, so a Basic Multicellular Unit, BMU. The first strategy used a 2D methodology for each layer and the second one calculated the regions in all envelop. The surfaces were transformed in STL file format for allowing 3D printing. The application of Matlab's tool *stlwrite* was used to export the surface volume produced with the two strategies.

Strategy 1 (S1). This strategy is based on solving differential equations in two dimensions and applying the *isosurface* tool. Bone density values obtained by solving the differential equations model with finite differences are used to develop a mesh surface. This surface is converted into a binarized mesh using a binary algorithm and, finally, the STL file is obtained by applying the multidimensional arrays tool from Matlab® software. Strategy 2 (S2) solves the differential equations in three dimensions, and with the obtained three-dimensional matrix, an *isosurface* similar to the one produced in S1 is created.

For two dimensions (x and y), applying finite differences in Eq. (5) and (6), Eq. (8) and (9) represents the model used for this strategy:

$$\frac{C_{i,j}^{(n+1)} - C_{i,j}^{(n)}}{\Delta t} = \frac{k_{i,j}C_{i+1,j}^{(n)} - 2C_{i,j}^{(n)} + C_{i-1,j}^{(n)}}{\Delta x^2} (D_c) + \frac{k_{i,j}C_{i,j+1}^{(n)} - 2C_{i,j}^{(n)} + C_{i,j-1}^{(n)}}{\Delta y^2} (D_c) + \alpha_1 C(u, t)^{g^{11}} B(u, t)^{g^{21}} - \beta_1 C(u, t), \quad (8)$$

$$\frac{B_{i,j}^{(n+1)} - B_{i,j}^{(n)}}{\Delta t} = \frac{k_{i,j}B_{i+1,j}^{(n)} - 2B_{i,j}^{(n)} + B_{i-1,j}^{(n)}}{\Delta x^2} (D_c) + \frac{k_{i,j}B_{i,j+1}^{(n)} - 2B_{i,j}^{(n)} + B_{i,j-1}^{(n)}}{\Delta y^2} (D_c) + \alpha_2 C(u, t)^{g^{12}} B(u, t)^{g^{22}} - \beta_2 B(u, t). \quad (9)$$

These meshes at different times can be "stacked" using the *Marching cubes algorithm* (*isosurface* tool from Matlab®) to obtain a three-dimensional surface. Using these meshes in Eq. 6, also a mesh is produced for bone mass. This strategy, called here as Strategy 1, would correspond to cell migration in the z direction that would continuously produce an extracellular matrix.

Strategy 2. A second approach to obtaining an STL that mimics bone structure from bone remodeling would be to simply solve Eq. 5-7 in three dimensions applying finite differences. Strategy 2 (S2) obtained a three-dimensional matrix, an

isosurface similar to the one produced in S1 is obtained with the Eqs. 10 and 11 for the population of osteoclasts (C) and osteoblasts (B).

$$\begin{aligned} \frac{C_{i,j,k}^{(n+1)} - C_{i,j,k}^{(n)}}{\Delta t} = & \frac{k_{i,j}C_{i+1,j,k}^{(n)} - 2C_{i,j,k}^{(n)} + C_{i-1,j,k}^{(n)}}{\Delta x^2} (D_C) + \frac{k_{i,j}C_{i,j+1,k}^{(n)} - 2C_{i,j,k}^{(n)} + C_{i,j-1,k}^{(n)}}{\Delta y^2} (D_C) \\ & + \frac{k_{i,j}C_{i,j,k+1}^{(n)} - 2C_{i,j,k}^{(n)} + C_{i,j,k-1}^{(n)}}{\Delta z^2} (D_C) + \alpha_1 C(u,t)^{g11} B(u,t)^{g21} \\ & - \beta_1 C(u,t), \end{aligned} \quad (10)$$

$$\begin{aligned} \frac{B_{i,j}^{(n+1)} - B_{i,j}^{(n)}}{\Delta t} = & \frac{k_{i,j}B_{i+1,j,k}^{(n)} - 2B_{i,j,k}^{(n)} + B_{i-1,j,k}^{(n)}}{\Delta x^2} (D_B) + \frac{k_{i,j}B_{i,j+1,k}^{(n)} - 2B_{i,j,k}^{(n)} + B_{i,j-1,k}^{(n)}}{\Delta y^2} (D_B) \\ & + \frac{k_{i,j}B_{i,j,k+1}^{(n)} - 2B_{i,j,k}^{(n)} + B_{i,j,k-1}^{(n)}}{\Delta z^2} (D_B) + \alpha_2 C(u,t)^{g12} B(u,t)^{g22} \\ & - \beta_2 B(u,t). \end{aligned} \quad (11)$$

Numerical Application

Parameters for bone dynamic model. Table 1 shows the parameter values used in this article based in Ayati et al. [6]. The $g11$ value is different in a single cycle event, in this case is equal to 0.5 and for oscillatory changes the $g11$ value is equal to 1.1.

Table 1 – Summary of parameters used in the model.

Parameters	Description	Value
α_1	Production rate of osteoclasts	3 [day ⁻¹]
α_2	Production rate of osteoblasts	4 [day ⁻¹]
β_1	Apoptosis rate of osteoclasts	0,2 [day ⁻¹]
β_2	Apoptosis rate of osteoblasts	0,02 [day ⁻¹]
k_c	Rate of bone's resorption	0,45% [day ⁻¹]
k_B	Rate of bone's formation	0,0448% [day ⁻¹]
D_C	Diffusion coefficient of osteoclasts	1x10 ⁻⁶ [bone mass mm ⁻¹]
D_B	Diffusion coefficient of osteoblasts	1x10 ⁻⁶ [bone mass mm ⁻¹]
\underline{C}	Cell population of osteoclasts in steady-state	1.06 [cell mm ⁻¹]
\underline{B}	Cell population of osteoblasts in steady-state	212.13 [cell mm ⁻¹]
$g11$	Autocrine signaling factor of osteoclasts	0.5 [single] 1.1 [osc.] [dimensionless]
$g21$	Paracrine signaling factor of osteoclasts	-0.5 [dimensionless]
$g22$	Autocrine signaling factor of osteoblasts	0.0 [dimensionless]
$g12$	Paracrine signaling factor of osteoblasts	1.0 [dimensionless]

Temporal Part Analysis - Single Remodeling Cycle. A separate function was created in auxiliary file to solve the Ordinary Differential Equations using adaptative Runge-Kutta method (ode45) in 150 days (t in days). The results are shown in Fig. (1).

Figures 1a and 1b show that the addition of 10 active osteoclast cells led to a consequent increase in the number of osteoblasts, and consequently, the stabilization of the number of osteoclasts returns to a steady state.

Figure 1c represents the evolution on percentage of bone mass: according to the role of the cells has an initial drop, related to the consumption performed by osteoclasts, and slow reformulation, related to the increase in the number of active osteoblastic cells.

Temporal Part Resolution - Periodic Remodeling Cycles. The literature points out that the change of osteoclasts parameters can be used to obtain the periodic cycles of remodeling. Komarova *et al.* [1] investigated the influence of each parameter on the stability and type of steady state obtained: the authors show the protagonist of the autocrine factor of osteoclasts (g_{11}); also, others authors point the same argument [14], [15]. Low g_{11} values reproduced only one remodeling cycle, while values greater than 1.1 lead to a dynamic remodeling with oscillations with increasingly higher amplitudes. These results were therefore obtained in Figs. 1d, 1e, and 1f, below, where a progressive variation in cell number and mass is evident. Therefore, changing the model constants to obtain a non-stationary response applying the adaptative Runge-Kutta's method analogously can be seen in Fig. 1d, 1e and 1f.

The initial value problem for this ODE system can exemplify the bone remodeling mechanism. However, the bone mass distribution is only for a single BMU. Ayati *et al.* [6], Valério *et al.* [7] and Fernández-Cervantez *et al.* [9] solved the presented model by adding a diffusive term for cell population and bone mass shown in Eqs. 7-10.

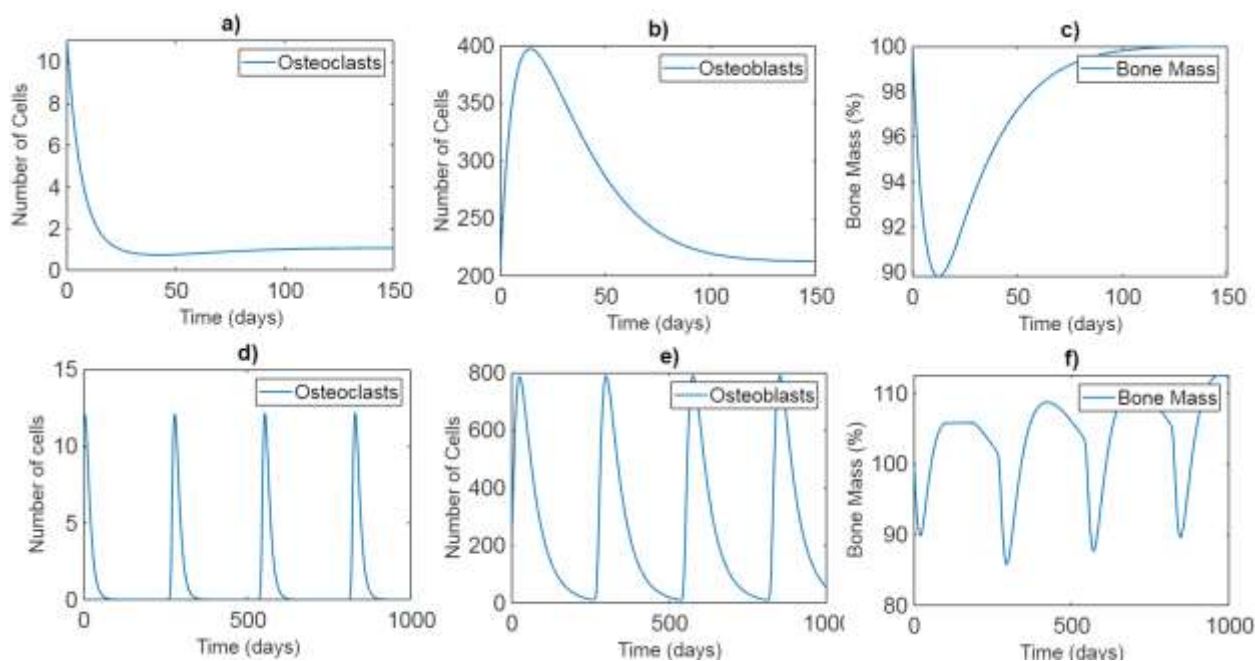


Figure 1 – Response to a bone remodeling cycle with the respective cellular behavior of osteoclasts (a), osteoblasts (b), and bone mass variation (c) and to periodic bone remodeling cycles with the respective behavior of osteoclasts (d), osteoblasts (e), and bone mass variation (f).

Different BMUs were evaluated at each point of a given mesh or solid block. The approach of Valério *et al.* [7,9] and Fernández-Cervantez *et al.* [9] were replicated below, in the respective Strategies 1 and 2. While in Strategy 1 the cell distribution is solved in x and y , in Strategy 2 it is solved in x , y and z . In order to obtain a three-dimensional block with the structure of trabecular bone, in the first form, therefore, it was necessary to apply the Multidimensional Matrices technique and the application of the *isosurface* tool after binarizing the data of each mesh x and y . In the second strategy, the matrix obtained already had orientations in three dimensions, which allowed the direct application of the *isosurface* tool, and binarizing the volume.

Resolution Space Part - Strategy 1. The addition of a diffusive term to the bone cell remodeling model proposed by Ayati *et al.* [6] allowed the assessment of cell population distribution and bone mass. Therefore, the non-trivial steady-state conditions obtained in the temporal resolution (previous item) are defined for the temporal part of the model. The diffusive part is solved using finite differences, as follows. By defining a remodeling time in a series of meshes with different initial conditions the parameters are defined for a time of 150 days. Fig. 2 shows the distribution grids for the final time of 150 days for cell populations and bone mass. In this figure we can see the distribution of cells in different areas, that is, where there are osteoclasts there is less population of osteoblasts, Figs. 2a and 2b. Also, denser regions could be seen in Fig. 2c areas with presence of osteoblasts, and less dense regions could be seen in populated osteoclasts areas. A loop was used in this case, with $dt = 0.01$ days

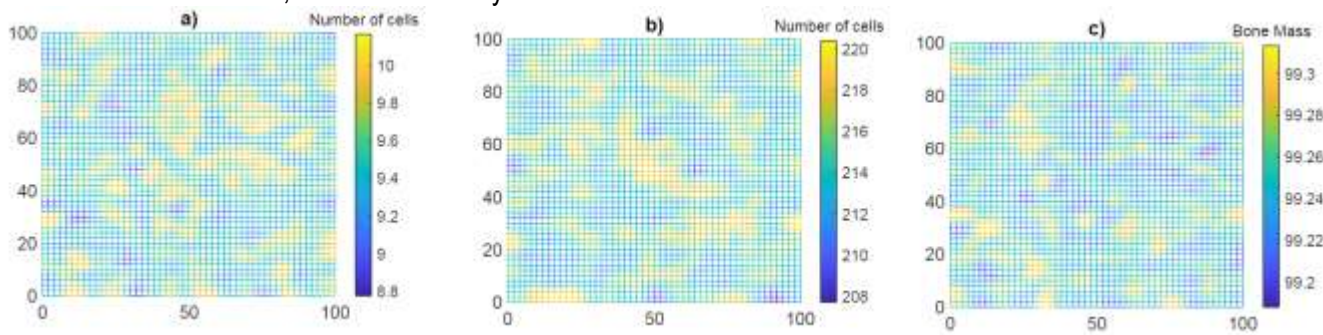


Figure 2 – Distribution of the cell population of osteoclasts (a), osteoblasts (b) and bone mass (c) with S1.

Resolution Spatial Part - Strategy 2. Strategy 2 only proposes solving for x, y, and z dimensions and plotting an isosurface from the volumetric data produced at $t = 150$. It assumes the same conditions as Strategy 2: a series of meshes with different initial conditions (different amounts of cells).

The distributions of cell populations and bone mass can be obtained as shown in Fig. 3. This figure shows the three-dimensional distribution of cells and bone mass. As consideration of *isosurfaces* produced: the marching cubes algorithm connects areas with the same value (defined as *isovalue*). For this, the data was binarized (a 3D Matrix of zeros and ones) to produce the isosurface in Fig. 3c. The *stlwrite* algorithm in Matlab was applied in order to export the STL files.

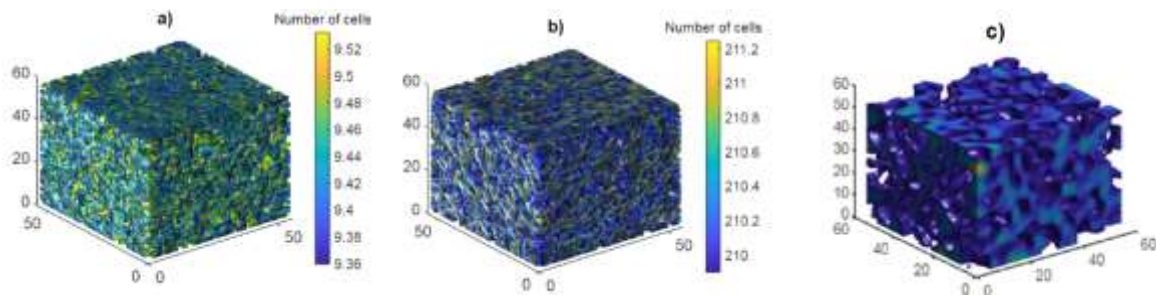


Figure 3 – Distribution of the cell population of osteoclasts (a), osteoblasts (b) and bone distribution (c) generated by Strategy 2 (dimensionless) in 150 days.

Analysis of 3D Printed pieces

Experimental Setup. The pieces were printed using the 3D Printer by FFF Dual Extruder N2 (Raise3D, Tesla, USA) for S1 and the Ultimaker 2+ for S2 (Ultimaker, Netherlands). The printing conditions were: nozzle temperature of 220°C, layer height of 0.15 mm, bed temperature of 60°C and printing speed of 5 mm/s (S1) and 60 mm/s (S2). The pieces were analyzed by microtomography using the equipment Easytom 130 (RX solutions, France) in Institut Clément Ader to obtain the microCT images.

Microtomography analyses. The application of microtomography (microCT) of the printed pieces allowed the complete geometry of the manufactured workpieces. Fig. 4 shows the microCT images of the S1 (Fig. 4a), S2 (Fig. 4b) and of real bone (femoral head (FH) gently provided by the National Institute of Technology (INT-Brazil), Fig. 4c).

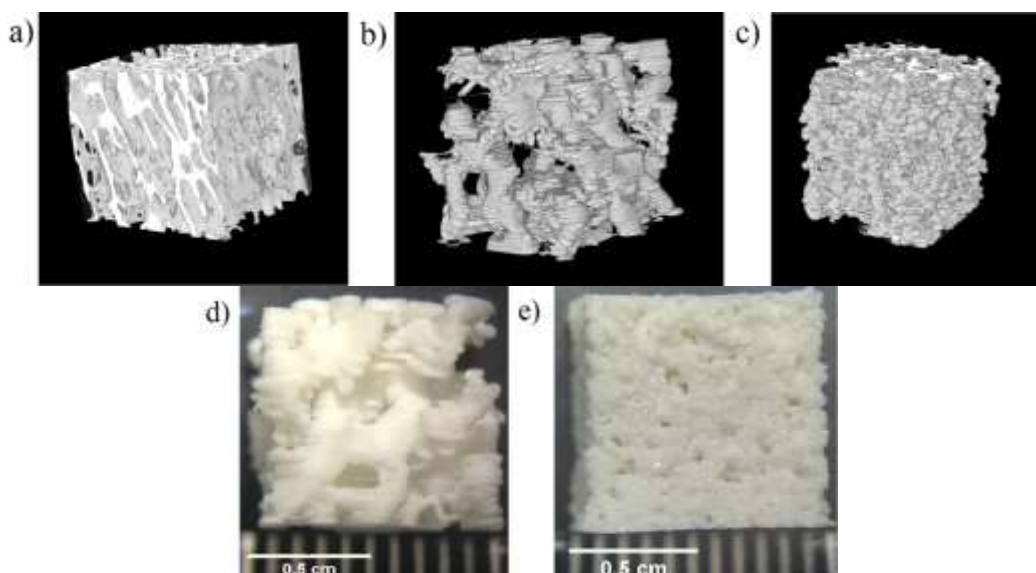


Figure 4 – MicroCT images obtained of the printed pieces with the different strategies: a) femoral head bone, b) S1, c) S2; the macrographs of the printed pieces: d) S1 and e) S2 obtained with magnifying glass (scale in cm).

The Bone J (ImageJ software plugin) was used in these analysis to obtain the parameters: trabecular thickness (TbTh, usually a mean value of thickness of the trabecula), trabecular separation (TbSp, the mean distance between the trabecula, it is similar to pore size), bone volume fraction (BV/TV, the fraction of material in the sample), degree of anisotropy (DA, it estimates how geometrically non-isotropic is the bone fraction), and connectivity (Conn, it gives an estimate of the number of connected trabeculae in the image) [11], [13].

The procedure to analyze the microCT images obtain were using the following image processing: no local means, unsharp mask, cropping image, binarize (Huang's method) and then use Bone J tool in the binarized images. For comparison, the microtomography of the femoral head (FH) bone also was characterized using the tool BoneJ. The choose of this kind of bone was because the parameters evaluated that could be printed by FFF was of this type of trabecular bone [10]. It is visible that pore size (TbSp) in S1 is greater than in real bone (FH). Some isotropy in z axes could be seen in Fig. 4a (FH). The morphology in S2 is closer of real bone, but the layers of 3D printing FFF technique misleading the accuracy.

Table 2 – Bone parameters obtained with BoneJ of microCT images.

Strategy	TbTh (mm)	TbSp (mm)	BV/TV	DA	Conn.
S1	0.89±0.299	2.001±1.180	0.402	0.564	457.25
S2	0.418±0.165	0.946±0.432	0.323	0.657	2663
FH	0.213±0.072	0.552±0.217	0.2940	0.688	617

The real bone data, trabecular femoral head bone, is near that observed in the literature [10] as seen in Table 2. However, the comparison of the strategies shows that median values are greater than real bone. Peyroteo *et al.* [8] with the same mathematical model implemented an algorithm for density that could assess more precise thickness and separation between struts. Also, the distribution in the histogram in Fig. 5 can provide that the profile in the distribution of TbTh and TbSp in FH and S2 were closer. As seen in Fig. 5, the profile of distribution of TbTh and TbSp is closer than S1, and S1 has greater TbTh and TbSp. It is interesting to notice that DA in S2 is near of the real bone. Nevertheless, S1 seems different than the others probably because of the methodology of this strategy, a bone mesh growing in time and not on space.

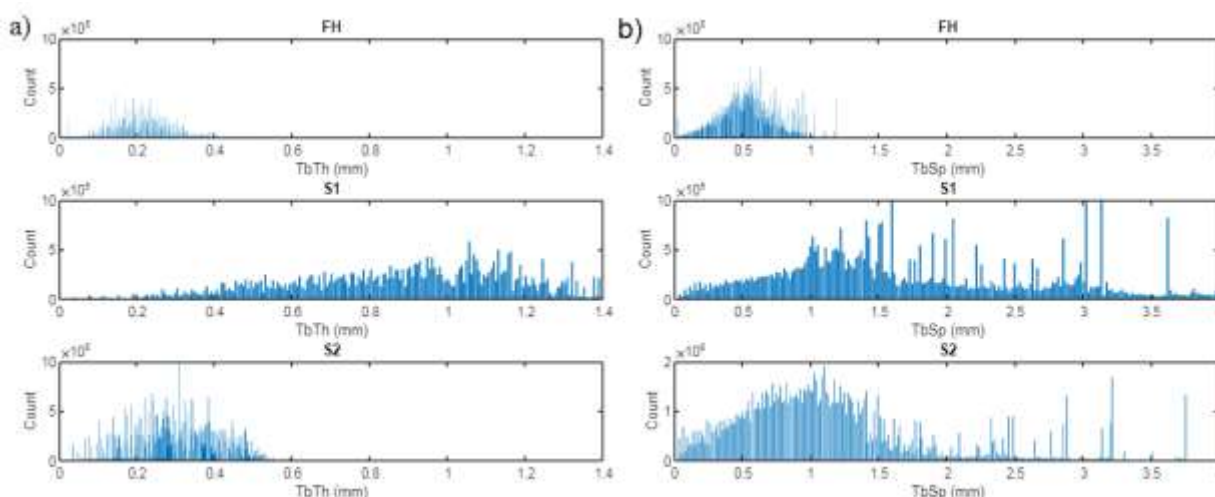


Figure 5 – Histograms for TbTh (a) and TbSp (b) for the different strategies and the femoral head bone.

Some modifications can be made in the algorithm proposed in methodology to reproduce exact profiles and morphological parameters, modifying some parameters in mathematical model and printing conditions. But it is interesting to notice that porosity and pore size (related to TbSp parameter) greater than in real bone morphology it is necessary to provide angiogenesis [3] and permeability of nutrients in damage tissue [16, 17]. Future works can search the biological response in these printed pieces geometries, in comparison with the gold standard [17] of architecture scaffolds in Bone Tissue Engineering.

Conclusions

This work reproduced the structure of trabecular bone using the mathematical model of cell dynamics. Pieces with trabecular architecture were successfully printed by FFF technique, a cheaper AM kind of 3D printer. It was possible to evaluate the most influential parameters of the human bone and compare real bone parameters and printed pieces via micro-computed tomography. Comparing morphologies S1 and S2, the average TbTh in S1 is double of S2. S2 was similar to FH in terms of the TbTh and TbSp about the profile distribution, although high variability in S2. DA, an important parameter for the angiogenesis, was closer in S2 than in S1 compared with FH. Therefore, the results here presented suggest that S2 can be applied to future works along with the optimization of the mathematical model and the printing parameters.

Acknowledges

The authors are grateful to Dra. Cristiane Evelise Ribeiro da Silva, researcher in INT – National Institute of Technology (Rio de Janeiro – Brazil), for gently providing the microtomography of the femoral head. Part of this work was produced during the mobility of Rossana Thiré as a Visiting Professor financed by INSA Toulouse in October 2023.

References

- [1] S. v. Komarova, R.J. Smith, S.J. Dixon, S.M. Sims, L.M. Wahl, Mathematical model predicts a critical role for osteoclast autocrine regulation in the control of bone remodeling, *Bone*. 33 (2003) 206–215. [https://doi.org/10.1016/S8756-3282\(03\)00157-1](https://doi.org/10.1016/S8756-3282(03)00157-1).
- [2] R. Florencio-Silva, G.R. da S. Sasso, E. Sasso-Cerri, M.J. Simões, P.S. Cerri, Biology of Bone Tissue: Structure, Function, and Factors That Influence Bone Cells, *Biomed Res Int*. 2015 (2015) 1–17. <https://doi.org/10.1155/2015/421746>.
- [3] M.N. Collins, G. Ren, K. Young, S. Pina, R.L. Reis, J.M. Oliveira, Scaffold Fabrication Technologies and Structure/Function Properties in Bone Tissue Engineering, *Adv Funct Mater*. 31 (2021) 2010609. <https://doi.org/10.1002/adfm.202010609>.
- [4] Z. Wood, L. Lynn, J.T. Nguyen, M.A. Black, M. Patel, M.M. Barak, Are we crying Wolff? 3D printed replicas of trabecular bone structure demonstrate higher stiffness and strength during off-axis loading, *Bone*. 127 (2019) 635–645. <https://doi.org/10.1016/j.bone.2019.08.002>.
- [5] C. Boyle, I.Y. Kim, Three-dimensional micro-level computational study of Wolff's law via trabecular bone remodeling in the human proximal femur using design space topology optimization, *J Biomech*. 44 (2011) 935–942. <https://doi.org/10.1016/j.jbiomech.2010.11.029>.
- [6] B.P. Ayati, C.M. Edwards, G.F. Webb, J.P. Wiksw, A mathematical model of bone remodeling dynamics for normal bone cell populations and myeloma bone disease, *Biol Direct*. 5 (2010) 1–17. <https://doi.org/10.1186/1745-6150-5-28>.
- [7] D. Valério, J. Neto, S. Vinga, Variable order 3D models of bone remodelling, *Bulletin of the Polish Academy of Sciences: Technical Sciences*. 67 (2019) 501–508. <https://doi.org/10.24425/bpasts.2019.129649>.
- [8] M.M.A. Peyroteo, J. Belinha, L.M.J.S. Dinis, R.M.N. Jorge, Bone remodeling: an improved spatiotemporal mathematical model, *Archive of Applied Mechanics*. 90 (2020) 635–649. <https://doi.org/10.1007/s00419-019-01631-z>.
- [9] I. Fernández-Cervantes, M.A. Morales, R. Agustín-Serrano, M. Cardenas-García, P. v. Pérez-Luna, B.L. Arroyo-Reyes, A. Maldonado-García, Polylactic acid/sodium alginate/hydroxyapatite composite scaffolds with trabecular tissue morphology designed by a bone remodeling model using 3D printing, *J Mater Sci*. 54 (2019) 9478–9496. <https://doi.org/10.1007/s10853-019-03537-1>.
- [10] M. McGregor, S. Patel, S. McLachlin, Mihaela Vlasea, Architectural bone parameters and the relationship to titanium lattice design for powder bed fusion additive manufacturing, *Addit Manuf*. 47 (2021) 102273. <https://doi.org/10.1016/j.addma.2021.102273>.
- [11] L. Steiner, A. Synek, D.H. Pahr, Comparison of different microCT-based morphology assessment tools using human trabecular bone, *Bone Rep*. 12 (2020) 100261. <https://doi.org/10.1016/j.bonr.2020.100261>.
- [12] S.C. Ligon, R. Liska, J. Stampfl, M. Gurr, R. Mülhaupt, Polymers for 3D Printing and Customized Additive Manufacturing, *Chem Rev*. 117 (2017) 10212–10290. <https://doi.org/10.1021/acs.chemrev.7b00074>.
- [13] J.F. Charles, A.O. Aliprantis, Osteoclasts: More than “bone eaters,” *Trends Mol Med*. 20 (2014) 449–459. <https://doi.org/10.1016/j.molmed.2014.06.001>.

- [14] R. Detsch, A.R. Boccaccini, The role of osteoclasts in bone tissue engineering, *J Tissue Eng Regen Med.* 9 (2015) 1133–1149. <https://doi.org/10.1002/term.1851>.
- [15] R. Domander, A.A. Felder, M. Doube, BoneJ2 - refactoring established research software, *Wellcome Open Res.* 6 (2021) 37. <https://doi.org/10.12688/wellcomeopenres.16619.2>.
- [16] B.N. Teixeira, P. Aprile, R.H. Mendonça, D.J. Kelly, R.M. da S.M. Thiré, Evaluation of bone marrow stem cell response to PLA scaffolds manufactured by 3D printing and coated with polydopamine and type I collagen, *J Biomed Mater Res B Appl Biomater.* 107 (2019) 37–49. <https://doi.org/10.1002/jbm.b.34093>.
- [17] H.B. Pan, Z.Y. Li, W.M. Lam, J.C. Wong, B.W. Darvell, K.D.K. Luk, W.W. Lu, Solubility of strontium-substituted apatite by solid titration, *Acta Biomater.* 5 (2009) 1678–1685. <https://doi.org/10.1016/j.actbio.2008.11.032>.